# Evaluation of a reduced mechanism for turbulent premixed combustion

CrossMark

Zacharias M. Nikolaou [a,*], Nedunchezhian Swaminathan [a], Jyh-Yuan Chen [b,1]

[a] Cambridge University, Department of Engineering, Trumpington Street, Cambridge CB2 1PZ, UK
[b] University of California at Berkeley, Department of Mechanical Engineering, 6163 Etcheverry Hall, Mailstop 1740, Berkeley, CA 94720-1740, USA

A B S T R A C T

In this study, 3D direct numerical simulations of a multi-component fuel consisting CO, $H_2$, $H_2O$, $CO_2$ and $CH_4$ reacting with air are performed. A freely propagating turbulent premixed stoichiometric flame is simulated for both low and high turbulence conditions i.e., the rms values of turbulent velocity fluctuations normalised by the laminar flame speed are of order 1 and 10. A skeletal mechanism involving 49 reactions and 15 species, and a 5-step reduced mechanism with 9 species, are used in order to evaluate the performance of the reduced mechanism under turbulent conditions. The 5-step mechanism incurs significantly lower computational expenses compared to the skeletal mechanism. The majority of species mean mass fractions and mean reaction rates computed using these two mechanisms are in good agreement with one another. The mean progress variable and heat release rate variations across the flame brush are also recovered by the reduced mechanism. No major differences are observed in flame response to curvature or strain effects induced by turbulence, although some differences are observed in instantaneous flame structure. These differences are studied using a correlation coefficient and detailed analysis suggests that this comes from the fluctuating heat release induced effects in the case with higher turbulence level. Further considerations based on instantaneous reaction rate and local displacement speed are discussed to evaluate the suitability of the reduced mechanism.

© 2014 The Combustion Institute. Published by Elsevier Inc. All rights reserved.

## 1. Introduction

Natural hydrocarbon based fuel resources such as methane are finite, and are becoming increasingly more expensive to extract often requiring off-shore drilling at great depths. At the same time emission regulations are becoming stricter, due to increasing levels of $CO_2$ in the atmosphere. In light of these developments, low calorific value fuels such as Coke Oven Gas (COG), Blast Furnace Gas (BFG), and those coming from bio-gasifiers, are becoming increasingly popular as alternative fuels for power generation using industrial gas-turbines [1]. These are typically multi-component fuels, involving CO, $H_2$, $H_2O$, $CH_4$, $CO_2$, $O_2$ and $N_2$, with their compositions varying greatly depending on the production process [2–4].

The design of combustors operating efficiently, and in an environmentally–friendly manner to burn such fuels in turbulent flows is challenging. An integral part of the modern design process involves computational fluid dynamics (CFD) simulations of turbulent reactive flows. Three-dimensional direct simulations of turbulent reactive flows of practical interest, are still expensive despite the development of faster and efficient computers. This is primarily

due to two issues: (1) accurate description of the flow field requires to resolve the smallest dissipative scales, i.e., the Kolmogorov scale $\eta_k$, which requires an extremely prohibitive fine numerical grid, and (2) accurate description of the chemistry, requires the use of a very large detailed reaction set. A detailed reaction set usually involves more than hundreds of reactions and tens of species, even for a simple fuel such as $CH_4$, and the requirement for multi-component fuels is even larger. Furthermore, the time scales associated with each species can be very disparate, thus requiring the use of an extremely small time-step. All of the above factors, make such simulations impractical even on the fastest super-computer available to date.

Reynolds averaged Navier–Stokes (RANS) and Large Eddy Simulations (LES) approaches tackle the first issue on numerical and computational requirements. The second issue on the required chemical complexity, can be tackled in a variety of ways, using tabulated chemistry approaches [5–10], and chemistry reduction involving quasi steady state assumptions (QSSA), combined with partial equilibrium assumptions [11–19]. In schemes with QSSA, the computational effort is reduced considerably by introducing steady-state and partial equilibrium assumptions for particular species and reactions respectively. This reduces the number of species to be carried in simulations and the stiffness of the system by removing species with relatively short lifetimes.

Usually, reduced mechanisms obtained using these approximations, are validated against laminar one-dimensional measurements such as the flame speed and ignition delay time. Following this validation procedure, such reduced mechanisms have been used in past Direct Numerical Simulation (DNS) studies [20–27], to gain insight for combustion sub-model development. This step entails a major assumption: that the reduced mechanism retains the same flame front structure and turbulence–flame interaction thereby yielding the same statistics as one would obtain using a detailed or a skeletal mechanism. This may or may not be correct and has not been validated yet in three dimensions, since most of the DNS studies in the past used either a single irreversible reaction or reduced chemical kinetics in three dimensional turbulence. Skeletal chemical kinetic mechanisms on the other hand were predominantly used in two dimensional simulations only, due to the high computational demand for three-dimensional simulations with detailed chemical complexity.

These investigations have been reviewed in many past studies [28–31], helping us to understand the role of chemical detail in turbulent combustion simulations. For example, it was shown in the 2D DNS of Baum et al. [32,33] that the responses of heat release rate and flamelet speed to curvature and tangential strain rate induced by turbulence on hydrogen–air premixed flames, were substantially different when a single or skeletal chemistry was used, although the general statistics such as the probability density function (pdf) of curvature did not vary much. The role of simulation dimensions was examined in detail in [34] where 2D simulations yielded much broader displacement speed pdfs in comparison with 3D simulations, with the discrepancies being proportional to the turbulence level $u_{rms}/s_l$, where $s_l$ is the laminar flame speed. While the 3D simulations revealed the displacement speed to be strongly negatively correlated with curvature, the 2D data showed a much weaker correlation [34]. Since the displacement speed strongly depends on the flow field and mixture transport properties, it is expected that the type of chemical mechanism used will also affect this correlation and the respective pdfs through turbulence–chemistry interaction. This is particularly important from a modelling point of view since the displacement speed is involved in the G-equation and FSD modelling approaches. Furthermore, preferential diffusion effects of light species, are not described when a 1-step chemistry is used. The comparison of LES results with experimental data to assess the accuracy of reduced chemistry models [35], suffers from many additional assumptions introduced for the sub-grid scale combustion modelling. As a result, the exact influence of the chemical model employed, cannot be isolated unambiguously.

DNS studies are ideal to isolate the influence of chemical kinetics modelling on the flame structure and turbulence–chemistry interaction, and to test the performance of a particular chemical scheme for turbulent combustion. However, in the past, DNS studies of premixed combustion in simple canonical configurations with skeletal chemistry and archetypical configurations with reduced chemistry were predominantly used to gain insights on turbulence–chemistry interaction and model validation. A review of these studies in [28] suggests that three-dimensional DNS with adequate detail of chemical kinetics will be required to make general strides on the development of combustion sub-models for optimal design of future engines and fuels. The DNS of combusting flows in archetypical configurations with detailed chemistry and molecular transport for multi-component fuels is expected to be beyond the reach of even exa-scale computing. The use of skeletal or reduced mechanisms seems a plausible choice at this time.

Obviously, a reduced mechanism is preferred for computational reasons. However, the reduced mechanism must retain the essential features of flame structure, the relative role of various fuel species and important radicals, and their interactions with turbulence. The former aspects are usually verified using laminar flame measurements and quantities computed using detailed or skeletal chemistry, as noted earlier. The turbulence–flame interaction aspects are usually presumed to hold. In this study, an attempt has been made to verify the ability of a reduced mechanism to capture the turbulence–flame interaction and flame front structure compared to a skeletal mechanism. This is achieved by performing 3D DNS of turbulent premixed combustion of a multi-component fuel mixture in a canonical configuration. The combustion chemistry is modelled using an extensively validated skeletal and 5-step reduced mechanism for multi-component fuel mixtures [36]. The details of these two mechanisms are given later in Section 2.1. The specific objectives of this study are (1) to compare the spatial distribution of heat release rate and species mass fractions in turbulent premixed flames computed using the skeletal and reduced mechanisms, (2) to study the respective statistics of mass fractions, reaction rates etc. obtained using these two mechanisms and (3) to examine the flame statistics, specifically pdfs of flame curvature, displacement speed, tangential strain rate, stretch rate and generalised flame surface density (FSD) which is closely related to the scalar dissipation rate of the reaction progress variable. These quantities are involved in combustion modelling based on flamelets approach.

The rest of the paper is organized as follows. The mathematical background and the numerical implementation are presented in Section 2 along with the computational parameters and the chemical schemes used. The results are presented and discussed in Section 3, and conclusions are drawn in the final section.

## 2. Mathematical background

### 2.1. Governing equations and numerical method

The direct numerical simulations have been conducted using the SENGA2 code [37] which is a fully compressible code. The equations solved are those for the conservation of instantaneous mass, momentum, energy, and species mass fractions. These equations are written respectively as

$$\frac{\partial \rho}{\partial t} + \frac{\partial \rho u_k}{\partial x_k} = 0, \tag{1}$$

$$\frac{\partial \rho u_i}{\partial t} + \frac{\partial \rho u_k u_i}{\partial x_k} = -\frac{\partial p}{\partial x_i} + \frac{\partial \tau_{ki}}{\partial x_k}, \tag{2}$$

$$\frac{\partial \rho E}{\partial t} + \frac{\partial \rho u_k E}{\partial x_k} = -\frac{\partial p u_k}{\partial x_k} - \frac{\partial q_k}{\partial x_k} + \frac{\partial \tau_{km} u_m}{\partial x_k}, \tag{3}$$

and

$$\frac{\partial \rho Y_\alpha}{\partial t} + \frac{\partial \rho u_k Y_\alpha}{\partial x_k} = \dot{\omega}_\alpha - \frac{\partial \rho V_{\alpha,k} Y_\alpha}{\partial x_k}. \tag{4}$$

using common nomenclature. The symbol $\alpha$ denotes a species identifier. Further details of the above equations can be found in [37].

The thermal conductivity of the mixture, $\lambda$, is calculated using a relationship in [38], which is given as

$$\frac{\lambda}{C_p} = A_\lambda \left(\frac{T}{T_0}\right)^r \tag{5}$$

where $C_p$ is the specific heat capacity at constant pressure for the mixture. The model parameters are $A_\lambda = 2.6246 \times 10^{-5}$ kg m$^{-1}$ s$^{-1}$ and $r = 0.6859$. The dynamic viscosity, $\mu$, of the mixture is calculated by assuming a constant Prandtl number, Pr, through

$$\mu = \frac{\lambda}{C_p} \text{Pr} \tag{6}$$

From laminar unstrained flame calculations Pr = 0.7. The diffusion velocities for species are calculated using Fick's law:

$$\rho V_{\alpha,k} Y_\alpha = -\rho D_\alpha \frac{\partial Y_\alpha}{\partial x_k}. \tag{7}$$

and the mass diffusivity, $D_\alpha$, for species $\alpha$ is calculated using [38]:

$$D_\alpha = \frac{\lambda}{\rho C_p Le_\alpha} \tag{8}$$

where $Le_\alpha$ is the Lewis number of species $\alpha$, which is taken to be constant but different for each species. These values calculated by taking the average $Le_\alpha$ for each species across the laminar unstrained flame are shown in Table 1.

The chemical reaction rate of species $\alpha$, $\dot\omega_\alpha$, is modelled using Arrhenious rate kinetics for 49 reactions involved in a skeletal mechanism [36] given in Table 2. This mechanism involves 15 species listed in Table 1 and it is suitable for combustion of low-calorific value multi-component fuel mixtures. This mechanism was validated in an earlier study [36] for a range of thermo-chemical conditions including laminar flame speeds and ignition delay times.

## 2.2. Development of reduced chemistry

The 5-step reduced mechanism was developed in [36] from the skeletal mechanism in Table 2, using the CARM software [39], which has the ability to directly generate source codes for the steady-state species reaction rates. By removing certain intermediate species from the skeletal mechanism, the computational effort is reduced as the number of non-steady state species to be carried in the simulations is decreased. For a restricted regime of interest, many intermediate species can be removed from the system without losing the solution accuracy. Such a reduced mechanism with QSSA, in the absence of transport phenomena, can be described as follows.

For non-QSS species:

$$\frac{\partial C_i}{\partial t} = \dot\omega_{ip} - \dot\omega_{id}, \quad i = 1 \ldots N_{s,\text{reduced}} \tag{9}$$

For QSS species:

$$0 = \dot\omega_{jp} - \dot\omega_{jd}, \quad j = 1 \ldots (N_{s,\text{skeletal}} - N_{s,\text{reduced}}). \tag{10}$$

The QSSA is applicable to an intermediate species when its production rate, $\dot\omega_{jp}$, is nearly equal in magnitude to the destruction rate, $\dot\omega_{jd}$, resulting in a very small net change in concentration. Concentrations of QSS species are solved by the non-linear algebraic system described in Eq. (10) without any truncation and are identified using a relative error based on their production and destruction rates, whereas non-QSS species concentrations are resolved in the usual manner using Eq. (9). Computational time saving results from a further decrease in system size from $N_{s,\text{skeletal}}$ to $N_{s,\text{reduced}}$. Furthermore, the stiffness of the system is also decreased as species with small life times are removed using a targeted search algorithm

**Table 1**
Species Lewis numbers. The species in parentheses are those in steady-state for the 5-step reduced mechanism.

| Index | Species | Le |
|---|---|---|
| 1 | H | 0.156 |
| 2 | $O_2$ | 0.996 |
| 3 | $H_2O$ | 0.756 |
| 4 | CO | 0.991 |
| 5 | $CO_2$ | 1.311 |
| 6 | $H_2$ | 0.264 |
| 7 | $H_2O_2$ | 1.005 |
| 8 | (OH) | 0.650 |
| 9 | ($HO_2$) | 0.998 |
| 10 | (HCO) | 1.149 |
| 11 | (O) | 0.637 |
| 12 | $CH_4$ | 0.896 |
| 13 | ($CH_3$) | 0.891 |
| 14 | ($CH_2O$) | 1.159 |
| 15 | $N_2$ | 0.922 |

**Table 2**
The skeletal mechanism. Units are in cm, s, mol, cal, K.

| | Reaction | A | n | Ea |
|---|---|---|---|---|
| 1 | $H + O_2 = O + OH$ | 2.650E+16 | −0.6707 | 17041.0 |
| 2 | $O + H_2 = H + OH$ | 3.870E+04 | 2.7 | 6260.0 |
| 3 | $OH + H_2 = H + H_2O$ | 2.160E+08 | 1.51 | 3430.0 |
| 4 | $2OH = O + H_2O$ | 3.570E+04 | 2.4 | −2110.0 |
| 5[a] | $H + O_2 + M = HO_2 + M$ | 2.800E+18 | −0.86 | 0.0 |
| 6 | $H + O_2 + H_2O = HO_2 + H_2O$ | 1.126E+19 | −0.76 | 0.0 |
| 7 | $H + O_2 + N_2 = HO_2 + N_2$ | 2.535E+19 | −1.3392 | 0.0 |
| 8 | $H + O_2 + He \Rightarrow HO_2 + He$ | 7.000E+17 | −0.8 | 0.0 |
| 9 | $H + O_2 + Ar \Rightarrow HO_2 + Ar$ | 7.000E+17 | −0.8 | 0.0 |
| 10 | $H + 2O_2 = HO_2 + O_2$ | 2.080E+19 | −1.24 | 0.0 |
| 11 | $H + HO_2 = 2OH$ | 8.316E+13 | 0 | 635.0 |
| 12 | $H + HO_2 = O_2 + H_2$ | 4.480E+13 | 0 | 1068.0 |
| 13(D) | $OH + HO_2 = O_2 + H_2O$ | 1.450E+13 | 0 | −500.0 |
| 14(D) | $OH + HO_2 = O_2 + H_2O$ | 5.000E+15 | 0 | 17330.0 |
| 15 | $H + HO_2 = O + H_2O$ | 3.970E+12 | 0 | 671.0 |
| 16 | $O + HO_2 = OH + O_2$ | 2.000E+13 | 0 | 0.0 |
| 17(D) | $2HO_2 = O_2 + H_2O_2$ | 1.300E+11 | 0 | −1630.0 |
| 18(D) | $2HO_2 = O_2 + H_2O_2$ | 4.200E+14 | 0 | 12000.0 |
| 19[b] | $2OH (+M) = H_2O_2(+M)$ | 7.400E+13 | −0.37 | 0.0 |
| 20 | $H + H_2O_2 = OH + H_2O$ | 1.000E+13 | 0 | 3600.0 |
| 21(D) | $OH + H_2O_2 = HO_2 + H_2O$ | 1.700E+18 | 0 | 29410.0 |
| 22(D) | $OH + H_2O_2 = HO_2 + H_2O$ | 2.000E+12 | 0 | 427.0 |
| 23 | $H + H_2O_2 = HO_2 + H_2$ | 1.210E+07 | 2 | 5200.0 |
| 24 | $O + H_2O_2 = OH + HO_2$ | 9.630E+06 | 2 | 4000.0 |
| 25[c] | $2H + M = H_2 + M$ | 1.000E+18 | −1 | 0.0 |
| 26 | $2H + H_2 = 2H_2$ | 9.000E+16 | −0.6 | 0.0 |
| 27 | $2H + CO_2 = H_2 + CO_2$ | 5.500E+20 | −2 | 0.0 |
| 28 | $2H + H_2O = H_2 + H_2O$ | 6.000E+19 | −1.25 | 0.0 |
| 29[d] | $H + OH + M = H_2O + M$ | 2.200E+22 | −2 | 0.0 |
| 30[e] | $2O + M = O_2 + M$ | 1.200E+17 | −1 | 0.0 |
| 31[f] | $O + H + M = OH + M$ | 5.000E+17 | −1 | 0.0 |
| 32 | $OH + CO = H + CO_2$ | 4.689E+07 | 1.228 | 70.0 |
| 33 | $HO_2 + CO = OH + CO_2$ | 1.500E+14 | 0 | 24544.0 |
| 34[g] | $O + CO (+M) = CO_2(+M)$ | 1.800E+10 | 0 | 2385.0 |
| 35 | $H + HCO = H_2 + CO$ | 7.340E+13 | 0 | 0.0 |
| 36 | $OH + HCO = H_2O + CO$ | 5.000E+13 | 0 | 0.0 |
| 37 | $HCO + O_2 = HO_2 + CO$ | 1.345E+13 | 0 | 400.0 |
| 38[h] | $HCO + M = H + CO + M$ | 1.870E+17 | −1 | 17000.0 |
| 39 | $HCO + H_2O = H + CO + H_2O$ | 1.500E+18 | −1 | 17000.0 |
| 40 | $O + HCO = H + CO_2$ | 3.000E+13 | 0 | 0.0 |
| 41 | $O + CH_4 = OH + CH_3$ | 1.020E+09 | 1.5 | 8600.0 |
| 42 | $OH + CH_4 = CH_3 + H_2O$ | 1.000E+08 | 1.6 | 3120.0 |
| 43 | $O + CH_3 = H + CH_2O$ | 5.060E+13 | 0 | 0.0 |
| 44 | $O + CH_3 \Rightarrow H + H_2 + CO$ | 3.370E+13 | 0 | 0.0 |
| 45 | $O + CH_2O = OH + HCO$ | 3.900E+13 | 0 | 3540.0 |
| 46[i] | $H + CH_3(+M) = CH_4(+M)$ | 1.390E+16 | −0.534 | 536.0 |
| 47 | $H + CH_4 = CH_3 + H_2$ | 6.600E+08 | 1.62 | 10840.0 |
| 48 | $H + CH_2O = HCO + H_2$ | 5.740E+07 | 1.9 | 2742.0 |
| 49 | $OH + CH_2O = HCO + H_2O$ | 3.430E+09 | 1.18 | −447.0 |

[a] $O_2/0.0$, $H_2O/0.0$, $CO/0.75$, $CO_2/1.5$, $N_2/0.0$, $Ar/0.0$, $He/0.0$.
[b] Low: 2.300E+18/−0.900/−1700.00, Troe: 0.7346/94.00/1756.00/5182.00, $H_2/2.0$, $H_2O/6.0$, $CH_4/2.0$, $CO/1.5$, $CO_2/2.0$, $Ar/0.7$, $He/0.7$.
[c] $H_2/0.0$, $H_2O/0.0$, $CH_4/2.0$, $CO_2/0.0$, $Ar/0.63$, $He/0.63$.
[d] $H_2/0.73$, $H_2O/3.65$, $CH_4/2.0$, $Ar/0.38$, $He/0.38$.
[e] $H_2/2.4$, $H_2O/15.4$, $CH_4/2.0$, $CO/1.75$, $CO_2/3.6$, $Ar/0.83$, $He/0.83$.
[f] $H_2/2.0$, $H_2O/6.0$, $CH_4/2.0$, $CO/1.5$, $CO_2/2.0$, $Ar/0.7$, $He/0.7$.
[g] Low: 6.020E+14/0.0/3000.00, $H_2/2.0$, $O_2/6.0$, $H_2O/6.0$, $CH_4/2.0$, $CO/1.5$, $CO_2/3.5$, $Ar/0.5$, $He/0.5$.
[h] $H_2/2.0$, $H_2O/0.0$, $CH_4/2.0$, $CO/1.5$, $CO_2/2.0$.
[i] Low: 2.620E+33/−4.760/2440.00, Troe: 0.7830/74.00/2941.00/6964.00, $H_2/2.0$, $H_2O/6.0$, $CH_4/3.0$, $CO/1.5$, $CO_2/2.0$, $Ar/0.7$, $He/0.7$.

(TSA) of Tham et al. [40]. Numerical solutions of the zero-dimensional Perfectly-Stirred Reactor (PSR) with the 49-reaction skeletal mechanism in Table 2 were used as input to CARM.

This reduced mechanism is written as:

(1) $O_2 + H_2O + 3CO \Rightarrow 2H + 3CO_2$

(2) $CO_2 + H_2 \Rightarrow H_2O + CO$

(3) $2H + CO_2 \Rightarrow H_2O + CO$

(4) $O_2 + 2H_2O + 2CO \Rightarrow 2H + 2CO_2 + H_2O_2$

(5) $2H + 4CO_2 + CH_4 \Rightarrow 3H_2O + 5CO$

and the rate expressions for the nine species involved in the above five steps are given in [36]. The supplementary material of this article provides a CHEMKIN compatible subroutine to calculate these reaction rates.

### 2.3. Flow configuration and boundary conditions

A sketch of the computational domain is given in Fig. 1. The computational domain is discretized in space using a structured Cartesian mesh. Each of the spatial derivatives in the conservation equations is evaluated at each mesh point using a 10th order central finite difference scheme for all interior points that are five or more points away from a non-periodic boundary. The order of this scheme is gradually reduced as the boundary is approached. Time advancement of the solution is carried out using a low-storage explicit five-stage fourth-order Runge–Kutta method [41]. The time-step size is 15 ns for all cases, determined by the acoustic CFL condition.

A freely propagating multi-component fuel premixed flame is simulated. At the inlet $\mathbf{u_{in}} = \bar{\mathbf{u}} + \mathbf{u}'$ where $\bar{\mathbf{u}} = (\bar{u}, 0, 0)$ is the constant mean inlet velocity and $\mathbf{u}'$ is the fluctuating turbulence velocity. These fluctuations are calculated from a pre-computed cold flow simulation using periodic boundary conditions and a Batchelor–Townsend energy spectrum. These pre-computed velocity fluctuations are then saved and added to mean flow at the inlet at every time step. A scanning plane runs through the saved velocity field and an interpolation scheme is used to update the inlet boundary.

Periodic boundary conditions are applied in the homogeneous $(y, z)$ directions. Subsonic constant density reflecting inflow boundary conditions are applied at the inflow boundary, and partially-reflecting boundary conditions at the outflow boundary, based on characteristics analysis [42,43], later extended to the NSCBC formulation [44]. Transverse convective terms are also included [45,46], in order to correctly estimate the wave amplitude variations at both the inflow and outflow boundaries. This was found to be an essential component to ensure numerical stability, especially for the highest turbulence level considered in this study.

### 2.4. Mixture conditions

The scalar field is initialised using a steady-state laminar flame solution obtained using the PREMIX code of the CHEMKIN package [47,48]. The fuel mixtu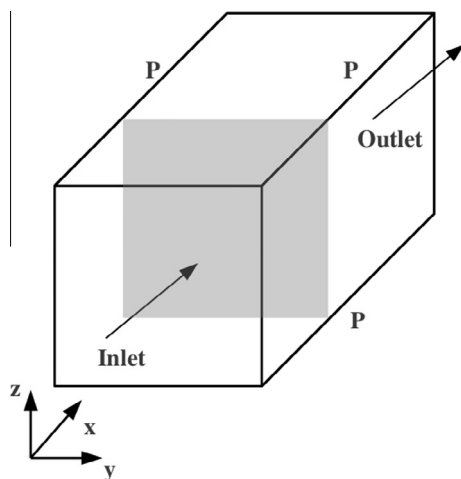re is at $T_r = 800$ K and 1 atm. It is composed of CO, $H_2$, $H_2O$, $CO_2$ and $CH_4$, and mole fraction percentages of these species are given in Table 3. This composition is typical of a BFG mixture [1], or a low hydrogen content syngas mixture [2–4]. At these conditions the laminar flame speed is $s_l = 2.5$ m/s and the flame thickness is $\delta_l = 0.75$ mm, where $\delta_l = (T_p - T_r)/\max(|dT/dx|)$, and $T_p$ is the product temperature.

### 2.5. Turbulent flame conditions

Table 4 lists the turbulence parameters used for the DNS: $u_{rms}$ is the root mean square value of fluctuating velocity, with an integral length scale $l_{int}$ on the reactant side. The turbulence Reynolds number is $Re = u_{rms}l_{int}/\nu_r$, where $\nu_r$ is the kinematic viscosity of the reactant mixture. The Damköhler number is $Da = (l_{int}/u_{rms})/(\delta/s_l)$, the Karlovitz number is $Ka = (\delta/\eta_k)^2$, and the Zeldovich thickness is defined as $\delta = \nu_r/s_l$. Figure 2 shows the locations of these conditions in the combustion diagram [49]. In order to isolate the effect of the turbulence level, the integral length scale is kept approximately the same. According to the classical combustion diagram [49], these conditions correspond to the thin reaction zones regime. The simulations were run for 9.76 and 2.56 flame times, $t_{fl} = \delta_l/s_l$, corresponding to about 34 and 32 eddy turn-over times, $t_e = l_{int}/u_{rms}$, for cases A and B respectively.

### 2.6. Computational requirements

The computational domain is $L_x = 14$ mm and $L_y = L_z = 7$ mm with the corresponding number of gridpoints $N_x = 768$ and $N_y = N_z = 384$ for cases A and B. For the 5-step reduced mechanism the same physical domain size and resolution is used for case B. The same physical domain size but with a smaller numerical res-

**Table 3**
Fuel mixture composition (molar percentages) used in the DNS. Note that the oxidizer is atmospheric air.

| $T_r$(K) | $\phi$ | $p$(atm) | CO | $H_2$ | $H_2O$ | $CO_2$ | $CH_4$ |
|---|---|---|---|---|---|---|---|
| 800.0 | 1.0 | 1.0 | 62.687 | 1.881 | 16.000 | 18.806 | 0.627 |

**Table 4**
Turbulence parameters for the DNS. $t_{tot}$ indicates the total run time of the simulations.

| Case | $u_{rms}/s_l$ | $l_{int}/\delta$ | Re | Da | Ka | $\bar{u}_{in}/s_l$ | $t_{tot}/t_{fl}$ | $t_{tot}/t_e$ |
|---|---|---|---|---|---|---|---|---|
| A | 3.18 | 16.54 | 52.66 | 5.19 | 1.39 | 2.6 | 9.76 | 33.92 |
| B | 9.00 | 16.66 | 150.05 | 1.85 | 6.62 | 3.6 | 2.56 | 31.99 |



**Fig. 1.** Sketch of the computational domain. Grey area indicates initial laminar flame.
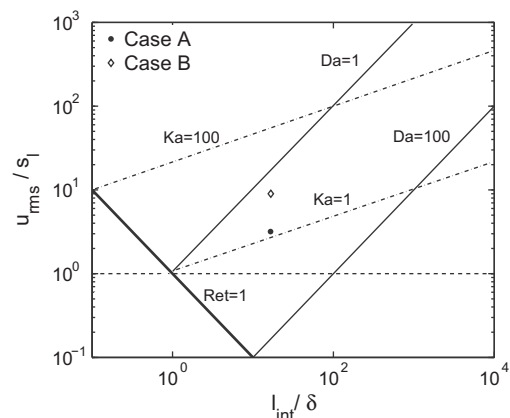


**Fig. 2.** Combustion regime diagram showing conditions of the two flames.

olution for the 5-step mechanism is used for case A having $N_x = 432$ and $N_y = N_z = 216$. The minimum reaction zone thickness among all species present namely $CH_4$ dictates the numerical resolution for case A, while the Kolmogorov length scale dictates the resolution for case B. It was observed that at least 20 points were required inside this minimum reaction zone thickness to ensure numerical stability for the skeletal mechanism, whereas for the 5-step reduced mechanism 10 grid points were sufficient to ensure this. The simulations were run on the UKs super-computer facility HECTOR. The computational details such as total memory requirements, number of cores used, output interval frequency, $t_{out}$, total number of sampled data sets, $N_{tot}$, and time step size, $\Delta_t$, are given in Table 5.

# 3. Results and discussion

## 3.1. Post-processing method

The global flame behaviour is analysed through the calculation of the consumption speed defined as:

$$s_c = \frac{-1}{\rho_r A} \int_V \frac{\sum_\alpha h_\alpha \dot{\omega}_\alpha}{C_p(T_p - T_r)} \, dV \qquad (11)$$

where $A$ is the total area in the homogeneous direction and the integral is taken over the volume $V$ of the computational domain. Figure 3 shows the temporal evolution of $s_c/s_l$ for the two cases. Time is normalized using the flame time $t_{fl}$ which is common for both cases. Initially $s_c$ is approximately equal to the laminar flame speed for both cases, indicating that $s_c$ is a good measure of global flame behaviour. After about one flame time, the flame reaches a statistically stationary state for case B and remains there up to 2.56 flame times where the simulation is stopped. Case A on the other hand shows a more delayed evolution: the consumption speed keeps increasing up to about 3 flame times and remains in

a more or less statistically stationary state up to about 5 flame times after which the consumption speed drops.

The DNS data have been post-processed using the same spatial differencing schemes as used in the DNS. Averaging is done both in space (in the homogeneous $y$, $z$ directions) and time, and by combining adjacent spatial points in order to increase the statistical accuracy. Five neighbouring points (symmetrically about $i$ for interior points) are combined after ensuring that the statistics such as the $x$-wise averages and the pdfs of $c$ are not unduly affected. The average value of a quantity $V$ at point $i$ in the $x$ direction is calculated using

$$\overline{V(i)} = \frac{1}{N_t N_y N_z N_p} \sum_{t=t_1}^{t=t_2} \sum_{k=1}^{N_z} \sum_{j=1}^{N_y} \sum_{p=1}^{N_p} V(i-3+p,j,k,t) \qquad (12)$$

where $N_p = 5$. The $i-3$ indicates that for points well away from the boundaries the averaging is symmetric about point $i$, using the 5 neighbouring grid points. Due care is taken at the boundaries. For case A, time averaging is performed between 3.5 and 5.6 flame times, and for case B time averaging is performed between 1 and 2 flame times. During these two intervals the flames in both cases seem to be in a statistically stationary state at least as far as $s_c$ is concerned as shown in Fig. 3. Conditional averages are taken over the entire volume in bins of $c$, and time-averaged over the above time intervals.

The flame surface except where stated otherwise is defined as the temperature iso-surface using $c = (T - T_r)/(T_p - T_r) = c^* = 0.32$, corresponding to the location of maximum heat release in the unstrained planar laminar flame. This choice is justified for this study because the discrepancies in statistics between the two mechanisms are observed to be maximum for $c$ close to $c^*$. Furthermore, mass fraction based progress variable definitions were shown in [50] to vary substantially among different reactant species. The $i$th component of a unit normal vector to the flame surface is given by

$$n_i = -\frac{1}{\chi} \frac{\partial c}{\partial x_i} \qquad (13)$$

where $\chi^2 = (\partial c/\partial x_i)(\partial c/\partial x_i)$, and the generalized fine-grained FSD is $\Sigma = \chi$. The flame stretch $\Phi$ is given by [51]

$$\Phi = (\delta_{ij} - n_i n_j) \frac{\partial u_i}{\partial x_j} + s_d \frac{\partial n_i}{\partial x_i} = a_t + s_d K_m \qquad (14)$$

where $a_t$ is the tangential strain rate, $K_m$ is the surface curvature, and $s_d$ the displacement speed. The displacement speed is calculated for all points on the flame surface using

$$\chi s_d = \frac{dc}{dt} = \frac{1}{\rho C_p} \frac{\partial}{\partial x_i} \left( \lambda \frac{\partial c}{\partial x_i} \right) - \frac{\partial c}{\partial x_i} \sum_a \frac{C_{pa} Y_a V_{ai}}{C_p} + \frac{\dot{Q}}{\rho C_p(T_p - T_r)} \qquad (15)$$

where the heat release rate is $\dot{Q} = -\sum_\alpha h_\alpha \dot{\omega}_\alpha$. The flame surface quantities are normalised as follows: $a_t^+ = a_t t_{fl}$, $K_m^+ = K_m \delta_l$ and $\Phi^+ = \Phi t_{fl}$.

Probability density functions of displacement speed, curvature, tangential strain and stretch are extracted from the flame surface calculated using the samples collected over the entire sampling period as for the mean quantities. These quantities are analysed to address the third objective of this study, but not all of these quantities are shown in this paper.

## 3.2. Comparison of spatial correlations

Figs. 4 and 5 show the instantaneous heat release rate in $x$–$y$ planes for cases A and B respectively. Slices are shown for four different $z^+$ spanning the entire length of the physical domain in the $z$ direction. The top row shows the results using the skeletal mecha-

**Table 5**
Computational requirements for the DNS. Cases in parentheses are with the reduced mechanism.

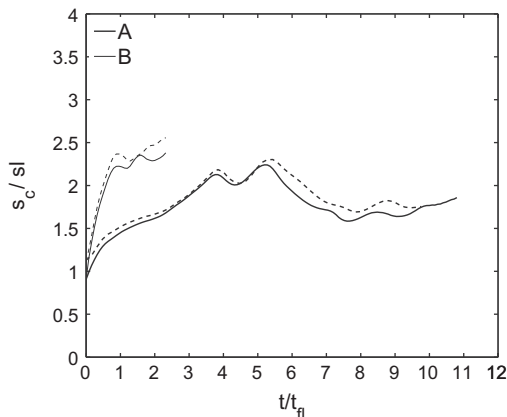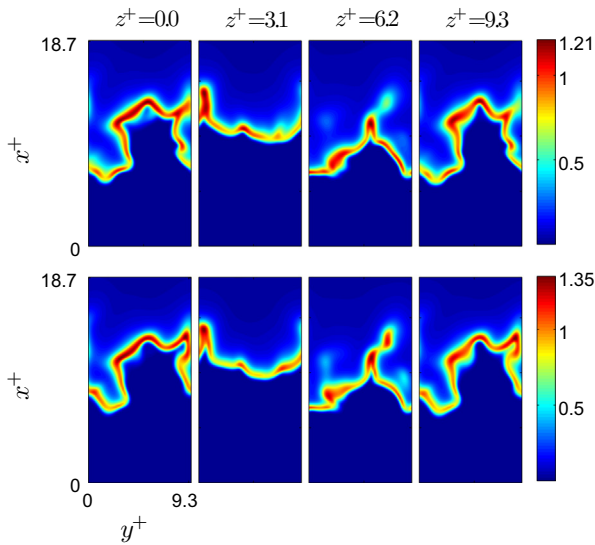| Case | Memory (GB) | Cores | Wall clock time (h) | $t_{out}/t_{fl}$ | $N_{tot}$ | $\Delta_t$ (ns) |
|------|-------------|-------|---------------------|------------------|-----------|-----------------|
| A | 304.1 | $24^3$ | 180 | 0.08 | 122 | 15 |
| (A) | 98.9 | $6^3$ | 240 | 0.08 | 122 | 15 |
| B | 304.1 | $24^3$ | 72 | 0.08 | 53 | 15 |
| (B) | 167.9 | $24^3$ | 36 | 0.08 | 53 | 15 |



**Fig. 3.** Consumption speed $s_c$ for cases A (thick line) and B (thin line), using the skeletal (continuous line) and reduced (dashed line) mechanisms.

**Fig. 4.** Instantaneous normalised heat release rate, $\dot{Q}^+$, in $x$–$y$ planes at different $z$ locations. Top row is for the skeletal mechanism and bottom row is for the reduced mechanism, for case A at $t/t_{fl} = 4$.
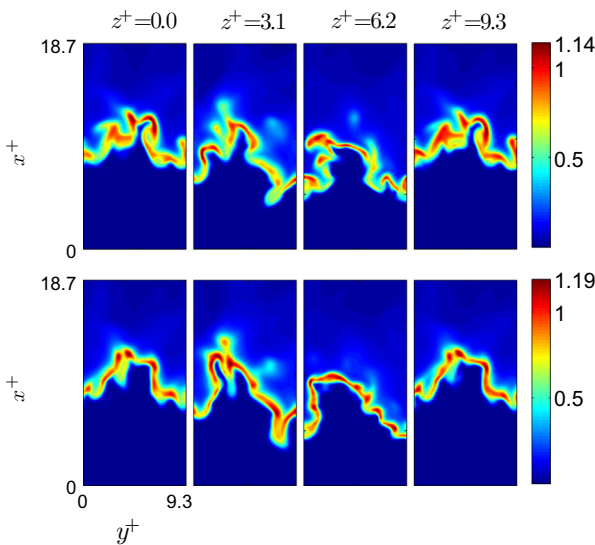


**Fig. 5.** Instantaneous normalised heat release rate, $\dot{Q}^+$, in $x$–$y$ planes at different $z$ locations. Top row is for the skeletal mechanism and bottom row is for the reduced mechanism, for case B at $t/t_{fl} = 1.6$.

nism, and the bottom row is for the reduced mechanism. The heat release rate $\dot{Q}$ in both figures is normalised using the maximum heat release rate in the laminar case for the skeletal mechanism, in order to highlight differences with the reduced mechanism.

For case A the general shape of the flame front is captured well by the reduced mechanism for all $z$. In both cases heat release is observed to peak in regions with negative curvature (convex towards the products), indicating that the same physical behaviour is recovered. Some differences are observed with respect to the maximum heat release rate values obtained, with the reduced mechanism reaching slightly higher maximum heat release values. Furthermore, heat release regions behind the "main" flame like the one for the third location, although captured with the reduced mechanism, are found to burn faster. For case B, the differences between the two mechanisms are more pronounced: the skeletal mechanism shows a more patchy and distributed flame front, giving an overall thicker flame. The reduced mechanism on the other

hand has a thinner flame front with a more continuous heat release zone. The difference though in the maximum heat release rate between the two mechanisms is reduced in comparison with case A, implying that turbulence is more dominant than chemical kinetics to the flame evolution.

The two-dimensional spatial cross-correlation function, $r$, can be used to better quantify the difference between the two mechanisms for a given $x^+$–$y^+$ plane. This can be calculated for each $z^+$ using

$$r(z_k) = \frac{\sum_i\sum_j\left(V^r_{ijk} - \overline{V^r}\right)\left(V^s_{ijk} - \overline{V^s}\right)}{\sqrt{\sum_i\sum_j\left(V^r_{ijk} - \overline{V^r}\right)^2\sum_i\sum_j\left(V^s_{ijk} - \overline{V^s}\right)^2}} \tag{16}$$

where $i$, $j$ and $k$ are indices for $x^+$, $y^+$ and $z^+$ directions respectively. The superscripts $s$ and $r$ stand for the skeletal and reduced mechanisms respectively. The over-bar indicates a two-dimensional average of a quantity $V$ in the corresponding $x^+$–$y^+$ plane. The cross-correlation, $r(z_k)$, is also time-averaged as discussed in the previous section and is calculated for the heat release rate and species mass fractions. The results are shown in Fig. 6 for cases A and B respectively. The correlation for the heat release rate is high for case A across all $z$, with the minimum falling only slightly below 0.8, a result consistent with the visual comparison seen in Fig. 4. For case B, the heat release correlation is not as strong and is found to drop to about 0.6 in the middle of the domain which is also in agreement with Fig. 4. A comparison of the corresponding correlations for the species mass fractions reveals strong correlations for H, $O_2$, CO, $CO_2$ and $CH_4$ with near 1 values. Furthermore, the species CO, $CO_2$ and $O_2$ have almost identical correlation distributions. These correlations are observed to be reduced for $H_2$, and the least strong correlations are observed for $H_2O$ and $H_2O_2$. The same pattern is found to be true for case B, with the difference that the correlations are in general weaker, except for $H_2$ whose correlation coefficient is less sensitive to the turbulence level.

In order to help elucidate the effect of the turbulence on the spatial correlations, Fig. 7 shows the correlation coefficients for the unstrained laminar flame. The correlation coefficients in the laminar case are all high contrary to the turbulent cases, reaching values larger than 0.9 both for the heat release and the species mass fractions. This result signifies the importance of using three-dimensional DNS data for validating the performance of a reduced mechanism, in contrast to laminar one-dimensional validations. Thus, turbulence reduces the spatial correlation coefficients through the influences of flame stretch and turbulence–chemistry interactions.

The 5-step mechanism was developed using numerical solutions of the Perfectly Stirred Reactor (PSR) to ease the numerical implementation, as input to CARM [39]. A species $\alpha$ was identified as being in steady-state if:

$$100 \cdot \frac{|\dot{\omega}_{\alpha p} - \dot{\omega}_{\alpha d}|}{\max(\dot{\omega}_{\alpha p}, \dot{\omega}_{\alpha d})} \leqslant e \tag{17}$$

where $\dot{\omega}_{\alpha p}$ and $\dot{\omega}_{\alpha d}$ are the species production and destruction rates respectively, and the error $e$ was taken to be less than 1%. Thus, are the poorer correlation coefficients observed in Fig. 6 in the turbulent case a result of the failure of the above QSS assumption related to the species rates? In order to establish the validity of this in the turbulent case, one can compute the maximum species rate-related QSSA error $e_\alpha$ from the skeletal chemistry DNS data using:

$$e_\alpha = \max_{gl}\left[100 \cdot \frac{(|\dot{\omega}_{\alpha p} - \dot{\omega}_{\alpha d}|)}{\max_{loc}(\dot{\omega}_{\alpha p}, \dot{\omega}_{\alpha d})}\right] \tag{18}$$

where the denominator is chosen based on the local maximum, $\max_{loc}$, between the species production and destruction rates, while the outer global maximum, $\max_{gl}$, is taken over the entire volume of
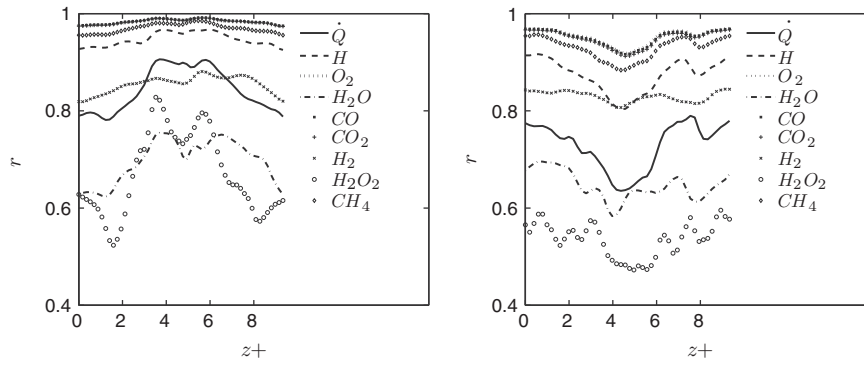
**Fig. 6.** Variation of correlation coefficient, $r$, with $z$ for $\dot{Q}$ and various species mass fractions, for case A (left) and case B (right).
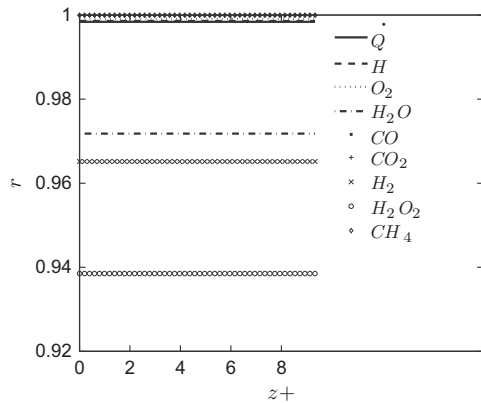


**Fig. 7.** Variation of correlation coefficient, $r$, with $z$ for $\dot{Q}$ and various species mass fractions, for the unstrained laminar flame.

the domain. Furthermore, in order to ensure that there are significant production or destruction rates for species $\alpha$ at the spatial point where the error is calculated, the denominator is subject to the following conditions. If the local production rate is larger than the local destruction rate i.e., $(\dot{\omega}_{\alpha p} - \dot{\omega}_{\alpha d}) \geqslant 0$, then

$$max_{loc}(\dot{\omega}_{\alpha p}, \dot{\omega}_{\alpha d}) = \begin{cases} \dot{\omega}_{\alpha p}, & \text{if } \dot{\omega}_{\alpha p} \geqslant 0.01 \times max_{gl}(\dot{\omega}_{\alpha p}) \\ \infty, & \text{otherwise} \end{cases} \quad (19)$$

If the local destruction rate is higher i.e., for $(\dot{\omega}_{\alpha d} - \dot{\omega}_{\alpha p}) > 0$, then

$$max_{loc}(\dot{\omega}_{\alpha p}, \dot{\omega}_{\alpha d}) = \begin{cases} \dot{\omega}_{\alpha d}, & \text{if } \dot{\omega}_{\alpha d} \geqslant 0.01 \times max_{gl}(\dot{\omega}_{\alpha d}) \\ \infty, & \text{otherwise} \end{cases} \quad (20)$$

Figure 8 shows the instantaneous $e_\alpha$ as obtained from the DNS using Eqs. (18)–(20) for species 1–14 in the skeletal mechanism (see Table 1), for cases A and B. A similar trend was observed at dif-

ferent time-steps. The laminar flame results are also shown as grey bars. It is important to remind ourselves at this point that species 8, 9, 10, 11, 13 and 14 i.e., OH, HO$_2$, HCO, O, CH$_3$ and CH$_2$O (see Table 1) are put in steady-state while developing the reduced mechanism [36]. Figure 8 shows that the errors for the laminar flame are larger than the 1% limit set in the PSR computations. Despite this, the use of the reduced mechanism is justified as the correlations in Fig. 7 are high. For cases A and B the error is reduced in comparison to the laminar flame for HCO only, and increased for OH, HO$_2$, O, CH$_3$ and CH$_2$O. Of these species, the steady-state assumptions introduced for OH, O, CH$_3$ and CH$_2$O are expected to primarily affect the CH$_4$ correlations, since these species readily interact with CH$_4$ through reactions 41–49 of Table 2. The spatial mass fraction correlations of CH$_4$ however in Fig. 6 are as high as in the laminar case, implying that CH$_4$ is relatively insensitive to the QSSA for the aforementioned species.

In order to understand how the rate-related QSSA error is affected by the turbulence, the local error, i.e., without the global maximum operation in Eq. (18) can be analysed. Figures 9–11 show $e_{OH}$, $e_{HO_2}$ and $e_O$ against $c$ for case B. These species readily react with H$_2$O and H$_2$O$_2$ in the majority of the reactions listed in Table 2, and are thus expected to impart the most influence on the spatial correlations for these species. Also shown in grey continuous lines is the QSSA error conditionally averaged in bins of $c$ and time-averaged as explained in Section 3.1. The grey dashed line shows the laminar flame result to elucidate the turbulence effect. In the laminar case, the QSSA error peaks at $c \simeq 0.5$ for OH, $c \simeq 0.01$ for HO$_2$ and $c \simeq 0.3$ for O. The local QSSA error for the turbulent case, on the other hand, peaks for all of these species at much lower $c$ values. This is expected since the turbulence is stronger at low $c$ values thus imparting most influence on species rates. As previously stated, the reduced mechanism was developed using PSR solutions as input to CARM, and as a result transport effects (convection and diffusion) are excluded. Hence stronger
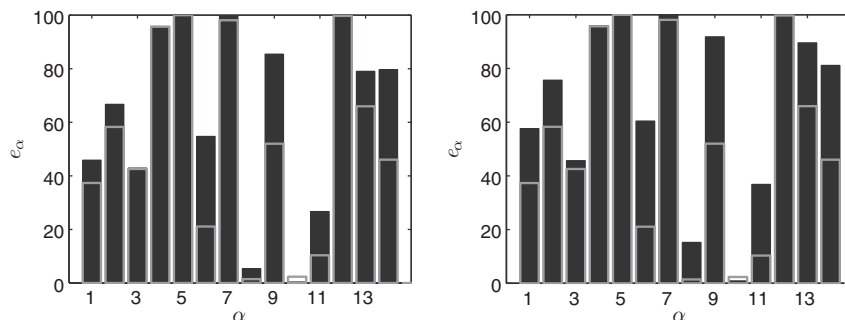


**Fig. 8.** Rate-related QSSA error, $e_\alpha$, for various species in Table 1. Case A result is shown on the left for $t/t_{fl} = 4.0$, and case B result is shown on the right for $t/t_{fl} = 1.6$. Grey bars show the laminar flame result.
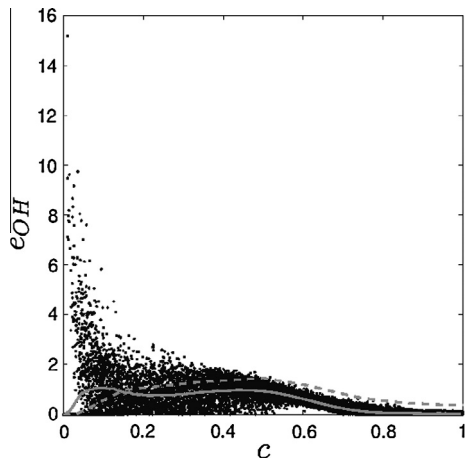
**Fig. 9.** Local QSSA error in percentage for OH. Grey continuous line: conditional average, conditioned on $c$ and time averaged. Grey dashed line: laminar flame result.
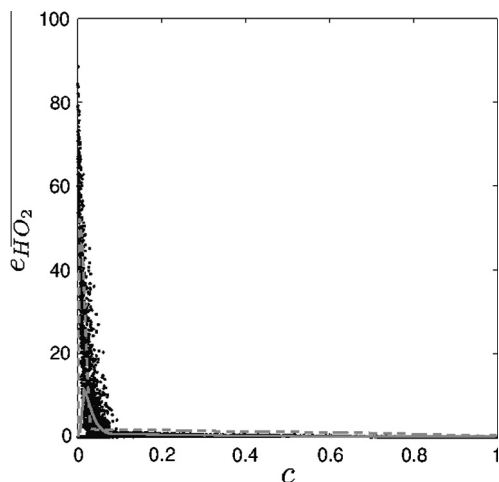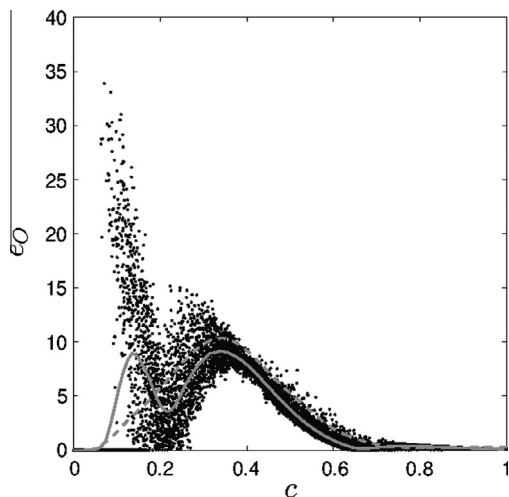


**Fig. 10.** Local QSSA error in percentage for $HO_2$. Grey continuous line: conditional average, conditioned on $c$ and time averaged. Grey dashed line: laminar flame result.



**Fig. 11.** Local QSSA error in percentage for O. Grey continuous line: conditional average, conditioned on $c$ and time averaged. Grey dashed line: laminar flame result.

turbulence for low $c$ values invalidates the QSSA through enhanced (turbulent) transport. On the burnt side the QSSA error is generally less since the turbulence is weaker. In particular, the conditional error is less than the laminar flame error for $c \geqslant 0.2$ for OH and O, and for $c \geqslant 0.1$ for $HO_2$. Also, for all of these species the majority of points fall below the laminar flame result implying that QSSA holds in the turbulent cases also. It is shown in the following sections that the mass fraction of $H_2O$ is over-estimated in a mean sense at relatively larger $c$ values. Since the conditional QSSA errors in Figs. 9–11 are larger than the laminar flame errors at relatively lower $c$ values, the low correlation observed for $H_2O$ at high $c$ values cannot be a result of the rate-related QSSA.

### 3.3. Comparison of mean profiles

In this section the mean profiles of important species mass fractions and net rates, heat release rate, and progress variable across the flame brush are examined, to test the performance of the 5-step reduced mechanism. The results are shown in Figs. 12–16. As noted earlier, the quantities are normalised using the maximum of laminar flame value for the skeletal mechanism. Figure 12 shows that the mean mass fraction of H is slightly under-estimated by the reduced mechanism as one moves towards the products, and close examination of Fig. 14 reveals that this is owing to the slight under-estimation of the H production rate over the same region. Nevertheless, taking into account that H is a highly diffusive species, the overall agreement with the skeletal mechanism is good. The CO mean mass fraction which is the main fuel constituent is well captured and similar results were found for the species $O_2$, $CO_2$ and $CH_4$. The mean mass fractions of $H_2O$ and $H_2O_2$ are over-estimated for both turbulence levels and the same was observed for the mean mass fraction of $H_2$, which explains the lower spatial correlations observed for these species in the previous section. Careful examination of Fig. 13 reveals that $H_2O$ and $H_2O_2$ are over-estimated in the unstrained laminar case also. $H_2O$ in particular is over-estimated mainly in the product side while $H_2O_2$ is over-estimated across the entire flame brush. Careful examination of Fig. 15 reveals that the over-estimation of the $H_2O$ mass fraction is owing to the over-estimation of its production rate in the same region. Similar arguments apply for $H_2O_2$ also, the only difference being that its consumption rate is instead over-estimated in the product side, which helps to explain why the reduced mechanism's estimation for the $H_2O_2$ mass fraction approaches that of the skeletal mechanism for large $x^+$.

As discussed in [36], these effects may be partly alleviated through the adjustment of the activation energy of one of the most dominant reactions, namely the chain-branching reaction $O + H_2 = H + OH$. Increasing the activation energy of this reaction would reduce the production rates of the OH and H radicals. This in turn would have a direct effect on the production rates and mass fractions of $H_2O$, $H_2$, and $H_2O_2$, since they readily interact with OH and H radicals. However, at the same time the flame speed would also decrease, since less OH radicals would be available for CO oxidation through the main heat releasing reaction $OH + CO = H + CO_2$. Since there is no way to pre-estimate the increase factor for the activation energy, this has to be based on one-dimensional laminar flame data. Thus, as it was indicated in [36], an increase of the activation energy of the reaction $O + H_2 = H + OH$ by 27.5%, reproduces the correct flame speed despite the small over-estimation of the aforementioned species mass fractions. Furthermore, species such as $CO_2$ (not shown here) relating to atmospheric pollution are estimated with excellent accuracy. Also, despite the discrepancies observed for the mean mass fractions of $H_2O$ and $H_2O_2$, as one may see from Fig. 16 the reduced mechanism captures very well the mean progress variable and heat release rate variation across the entire flame brush. For
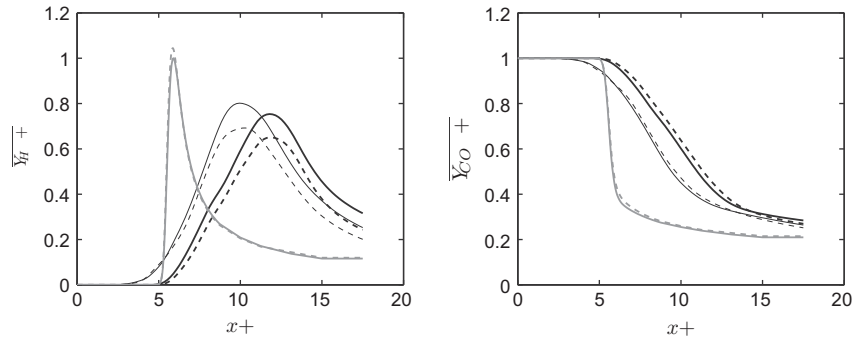
**Fig. 12.** Variations of H and CO mean mass fractions with $x^+$. Thick lines – case A, thin lines – case B. Continuous line is for skeletal mechanism and dashed line is for reduced mechanism. Grey lines are for unstrained laminar flames.
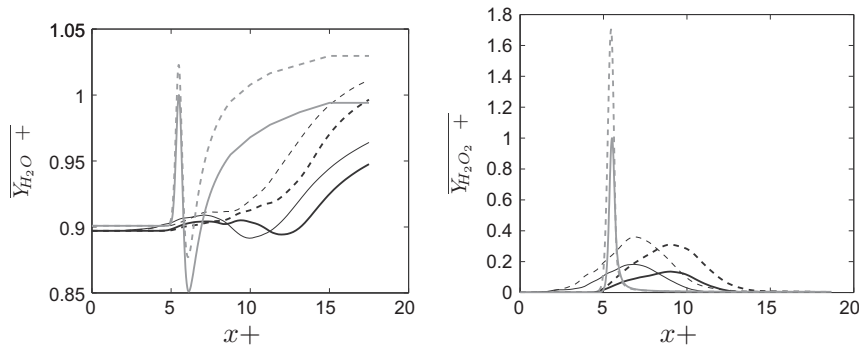


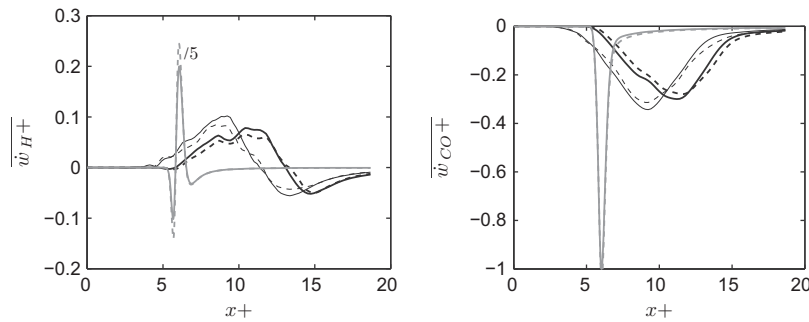**Fig. 13.** Variations of $H_2O$ and $H_2O_2$ mean mass fractions with $x^+$. Lines are as in Fig. 12.



**Fig. 14.** Variations of H and CO net mean reaction rates with $x^+$. Lines are as in Fig. 12.
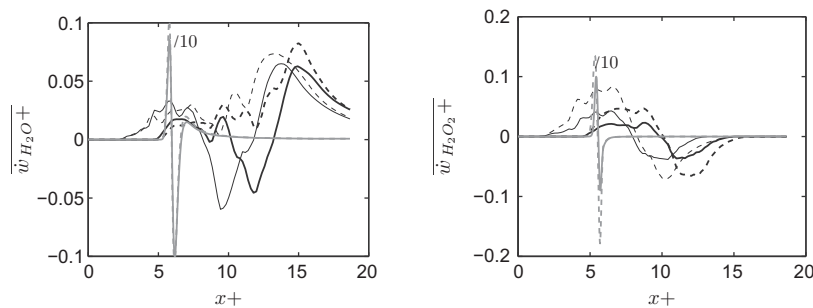


**Fig. 15.** Variations of $H_2O$ and $H_2O_2$ net mean reaction rates with $x^+$. Lines are as in Fig. 12.

both turbulence levels the reduced mechanism predicts the heat release rate to drop and spread out due to flame thickening and consistent with the laminar flame result, the maximum heat release rate occurs around $\bar{c} = 0.32$ also.

### 3.4. Comparison of flame front structure

The 5-step reduced mechanism was found in the previous section to give an overall good agreement with the majority of species
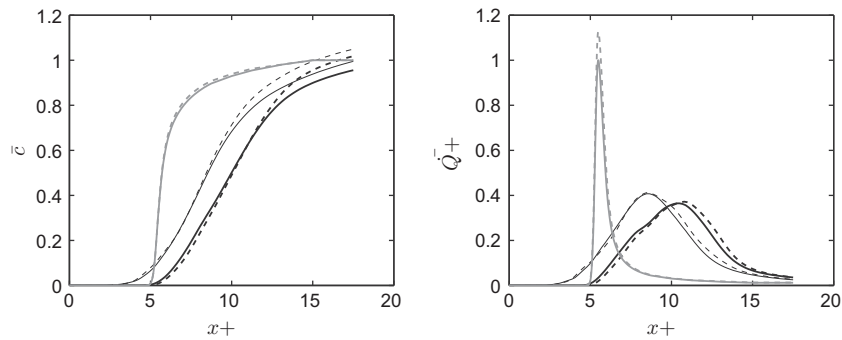
**Fig. 16.** Variations of mean $c$ and $\dot{Q}^+$ with $x^+$. Lines are as in Fig. 12.

mass fractions and heat release rate in the mean sense. From a modelling point of view, one would use the reduced mechanism DNS data not only to save computational time but also to develop combustion sub-models many of which are based on the flamelet assumption. The conditional averages give an indication of the flamelet nature of the turbulent flame. Thus, the conditionally averaged mass fractions and heat release rate are studied in this section.

Figs. 17–20 show conditional averages in bins of $c$ for the species mass fractions and heat release rate for the highest turbulence level, i.e., case B. Similar results were obtained for case A and thus they are not shown here. The continuous black lines show the results for the skeletal mechanism and the dashed black lines show the results for the reduced mechanism. Also the laminar flame result is shown using grey lines to elucidate the effect of the turbulence. Figure 17 shows that the conditionally averaged mass fractions of H and CO are well captured by the reduced mechanism and a similar good agreement was also found for the conditional averages of $O_2$, $CO_2$ and $CH_4$. These results imply that the distribution of the aforementioned species over the temperature field calculated with the reduced mechanism is similar to that using the skeletal mechanism. Figure 18 shows that the conditional average of the $H_2O$ mass fraction is estimated equally well as the H mass fraction. Nevertheless, for high $c$ which are expected to occur for large $x$, the conditionally averaged mass fraction of $H_2O$ is slightly over-estimated. This happens both for the laminar and the turbulent cases which explains the associated over-estimation of its mean spatial value for large $x$. Careful examination of the reactions involving $H_2O$ shows that one of the most important reactions affecting $H_2O$ concentration is the reaction $OH + H_2 = H + H_2O$. Furthermore, this reaction was found to become more important as one moves towards the products side and actually produces $H_2O$ for large $c$ [36,50,52,53].

Fig. 19 shows that the conditionally averaged mass fraction of $H_2$ is also over-estimated, and for all $c$ even in the laminar case.

Both the $H_2O$ and the $H_2$ over-estimation for the laminar flame are interlinked: the reaction $O + H_2 = H + OH$ affects the $H_2$ concentration significantly and throughout the flame brush. The QSSA for O and OH, causes higher reverse rates through this step, reducing the $H_2$ consumption, and increasing its concentration throughout. At the same time, the QSSA combined with the higher levels of $H_2$ enhances the forward rate of the reaction $OH + H_2 = H + H_2O$ at large $c$, producing more $H_2O$, and causing an over-estimation in its concentration in this region. However, as explained in Section 3.2, despite this fact the correlations in the laminar flame remain high. Furthermore, the $H_2O$ over-estimation occurs at large $c$ and as shown in Section 3.2 the QSSA (for the species expected to affect the most the $H_2O$ concentration) in the turbulent case, holds on average better in this region than in the laminar flame. Hence the lower spatial correlations for $H_2O$ observed in Fig. 6 in the turbulent case, are owing primarily to the different scalar–turbulence interaction rather than failure of the QSSA.

Fig. 18 also shows the conditional average of $H_2O_2$, which in comparison to $H_2O$ peaks at lower $c$ values. This explains the much lower spatial correlations observed for $H_2O_2$ in Figs. 6 and 7, since this species exhibits strong mass fraction gradients in regions of intense turbulence. As noted previously while discussing Figs. 9–11, the QSSA errors peak in the regions of low $c$ values. One would therefore expect, perhaps, the $H_2O_2$ over-estimation seen in Fig. 18 to be associated with failure of the QSSA. However, when compared to the laminar flame result, the over-estimation using the reduced mechanism, for the turbulent case at low $c$ is approximately of the same magnitude, implying that this is not resulting from the QSSA. Another important observation which may help to justify the above point is as follows: for $c \geqslant 0.2$, the difference with the skeletal mechanism result is small for the laminar case but it is large for the turbulent case. Figures 9–11 show that in the same range, i.e., for $c \geqslant 0.2$, the conditional QSSA error for OH, $HO_2$ and O is actually smaller than the laminar case despite the increased discrepancies in Fig. 18. Thus, the over-estimation
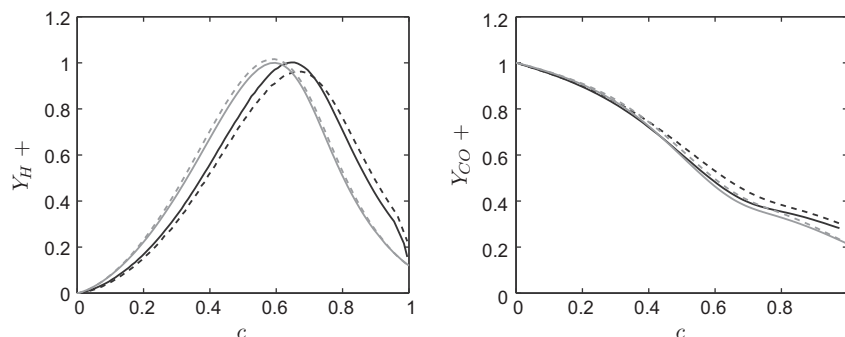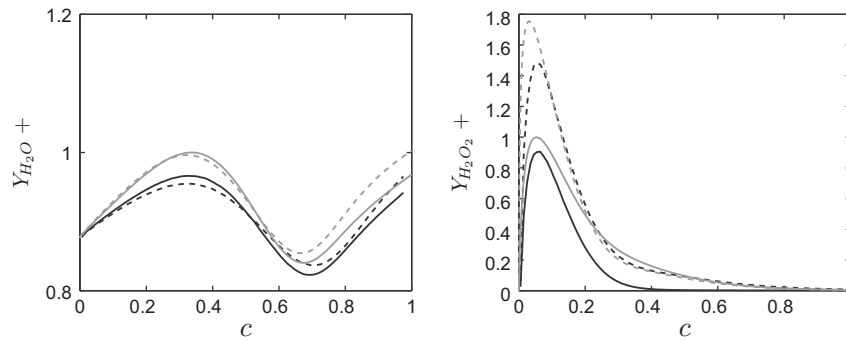


**Fig. 17.** H and CO mass fractions conditionally averaged in bins of $c$, and time-averaged for case B, using the skeletal (black continuous lines) and the reduced (black dashed lines) mechanisms. Grey lines show the unstrained laminar flame result.

**Fig. 18.** $H_2O$ and $H_2O_2$ mass fractions conditionally averaged in bins of $c$, and time-averaged for case B. Lines as in Fig. 17.
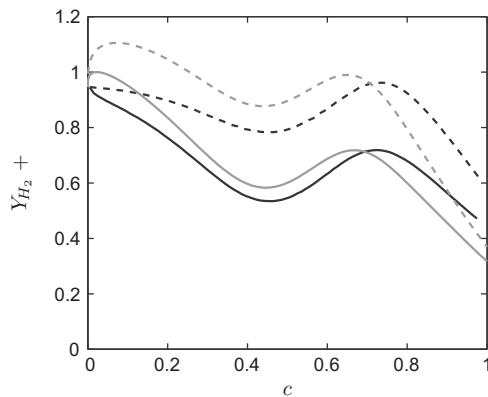


**Fig. 19.** $H_2$ mass fraction conditionally averaged in bins of $c$ and time-averaged for case B. Lines as in Fig. 17.
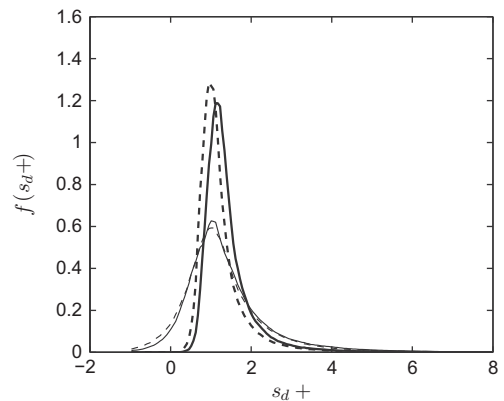


**Fig. 20.** Heat release rate conditionally averaged in bins of $c$ and time-averaged for case B. Lines as in Fig. 17.



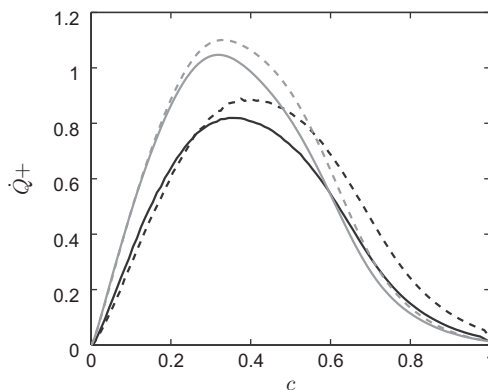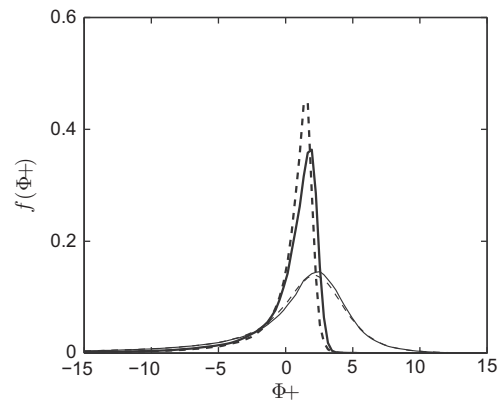**Fig. 21.** Surface displacement speed pdfs. Lines as in Fig. 12.



**Fig. 22.** Surface stretch pdf. Lines as in Fig. 12.

of the $H_2O_2$ mass fraction for the reduced mechanism in the turbulent case cannot be correlated to the failure of the QSSA, at least for the conditions investigated in this study.

Fig. 20 shows the conditionally averaged heat release rate. The values obtained using the 5-step reduced mechanism agree well those obtained using skeletal mechanism for small $c$ values. The reduced mechanism slightly over-estimates the conditionally averaged heat release rate for large $c$ values. This is consistent with the results shown in Fig. 5. Since most of the heat release comes from the enthalpy of formation of $H_2O$ whose mass fraction as previously discussed is over-estimated for large $c$, this causes the associated slight over-estimation of the heat release rate in the same region of $c$ space. Nevertheless, it is shown in the following section that the flame surface statistics obtained with the skeletal mechanism are recovered using the reduced mechanism.

### 3.5. Comparison of flame surface statistics

Figs. 21–23 show pdfs of the displacement speed, flame stretch and generalized FSD. These quantities are obtained on $c = 0.32$ iso-surface where the heat release rate peaks in the laminar flame. The pdfs of curvature and tangential strain rate using the reduced mechanism were indistinguishable with the skeletal mechanism results and thus they are not shown here. As one may see from Fig. 21, the reduced mechanism produces almost identical displacement speed pdfs with the skeletal mechanism both for the low and high turbulence levels. This implies that the flame structure computed using the reduced mechanism has the same dependency on strain and curvature effects as with that computed using the skeletal mechanism. Thus, the flame stretch is also almost
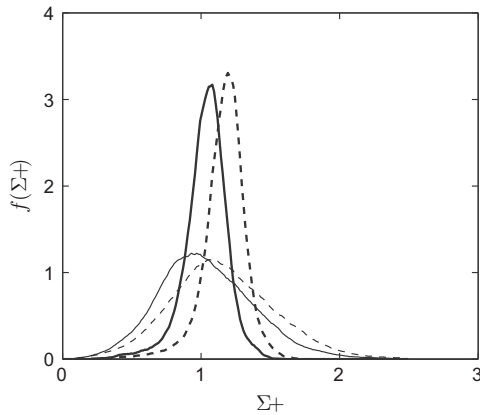
**Fig. 23.** Surface generalized FSD pdf. Lines as in Fig. 12.

identical for the reduced and skeletal mechanisms as one can observe in the flame stretch pdf shown in Fig. 22. The pdf of generalized fine-grained FSD shown in Fig. 23 suggests some differences. This quantity has a higher mean value for both turbulence levels when the reduced mechanism is used. Since $\Sigma_{gen} = \chi$, it is a measure of the flame front thickness and thus the reduced mechanism has a slightly thinner flame front. This implies that flame statistics obtained using the reduced mechanism is less sensitive to the turbulence level as observed in previous studies [32,33,54]. The quantitative difference, however, is found to be less than 12%.

Fig. 24 shows scatter plots for the heat release rate and displacement speed against curvature for case B. Similar results were observed for case A. The black dots are for the skeletal mechanism and the grey dots for the reduced mechanism. The expected physical behaviour, i.e., heat release rate and displacement speed correlate strongly with curvature and their peak values occurring in negatively curved regions, is recovered by the reduced mechanism for both turbulence levels. The results for both mechanisms are found to be nearly identical in regions of positive curvature. For negatively curved regions, the reduced mechanism slightly overestimates $\dot{Q}^+$ and $s_d^+$, which is consistent with the visual pictures shown in Figs. 4 and 5.

Fig. 25 shows the corresponding scatter plots for correlation with tangential strain rate. Although some correlation is observed for the heat release rate, with generally positively strained regions showing a higher heat release rate, the influence of curvature is much more dominant. The correlation between $s_d^+$ and $a_t^+$ is not as strong as for the heat release rate. The displacement speed is observed to reach a maximum for $a_t^+ > 0$. For large strain rates,

the displacement speed drops down to the laminar flame speed and shows the same dependency as for negatively strained regions. All of these effects are well captured by the reduced mechanism for both turbulence levels indicating that it is an acceptable substitute for the skeletal mechanism even for turbulent combustion.

### 3.6. Further consideration

From the above discussion in Sections 3.2–3.5, it is clear that the 5-step reduced mechanism can reproduce the flame statistics well. However, one can argue that the quantities studied in these sections are averaged and thus the averaging process can mask the effects of errors associated to QSSA, which form the premises for developing the reduced mechanism. There are two ways to assess this point in a broad perspective, one way is to have two different reduced mechanisms with significantly different reduction errors and a second method is to carefully study the instantaneous quantities, such as the flame front locations and heat release rate obtained using the reduced and skeletal mechanisms. Any chemistry reduction method will aim to minimise the reduction error which is related to a careful selection of species obeying QSSA within a carefully selected tolerance limit so that the reduced set can reproduce flame observables such as laminar burning velocity, flame thickness etc., and ignition delay times, which are either measured or computed using a skeletal/comprehensive mechanism. As noted earlier in Section 2.2, the 5-step reduced mechanism considered here was shown to reproduce these observables for a wide range of thermochemical conditions in [36]. It is also important to recognise that the first method will be helpful to answer a question such as, what is the sensitivity of the reduction error on the turbulent flame observable when a reduced chemistry is employed? Since the focus of this study is to assess the performance of the reduced 5-steps for turbulent flames invariably involving flame stretch, corrugations and contortions, the second method is used here for further assessment.

The flame front position at time $t$, evolved from an instant $t_1$, is given by

$$\mathbf{x}_f(t) = \mathbf{x}_f(t_1) + \int_{t_1}^{t} \left(\frac{d\mathbf{x}_f}{dt}\right) dt \qquad (21)$$

where

$$\frac{d\mathbf{x}_f}{dt} = \mathbf{u} + s_d\mathbf{n} = (\tilde{\mathbf{u}} + \mathbf{u}') + s_d\mathbf{n}. \qquad (22)$$

Thus, the temporal evolution of flame front position is controlled by a fine balance among the mean convection, turbulent fluctuating velocity, and the self propagation of the flame front denoted by the displacement speed $s_d$. The former two quantities are governed predominantly by fluid dynamics, which is kept to be the same for
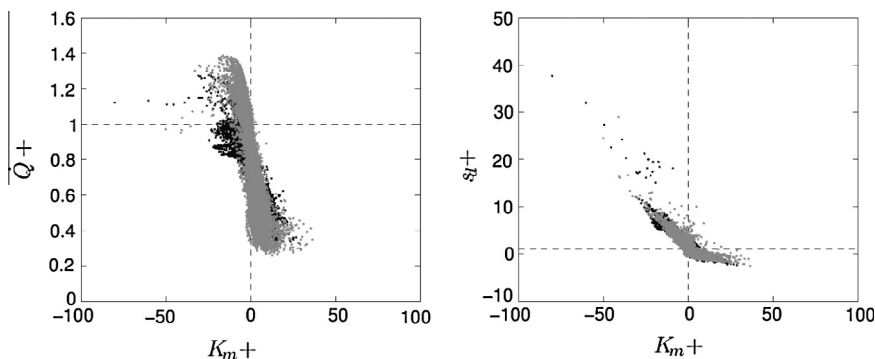


**Fig. 24.** Scatter plots of $\dot{Q}^+$ vs. $K_m^+$ and $s_d^+$ vs. $K_m^+$. Black symbol is for the skeletal and grey symbol is for the reduced mechanism. The results are shown for case B at $t/t_{fl} = 1.6$.
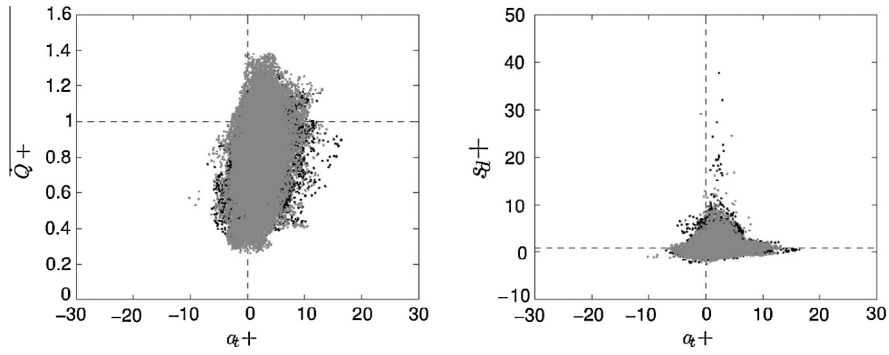
**Fig. 25.** Scatter plots of $\dot{Q}^+$ vs. $K_m^+$ and $s_d^+$ vs. $K_m^+$. Black symbol is for the skeletal and grey symbol is for the reduced mechanism. The results are shown for case B at $t/t_{fl} = 1.6$.
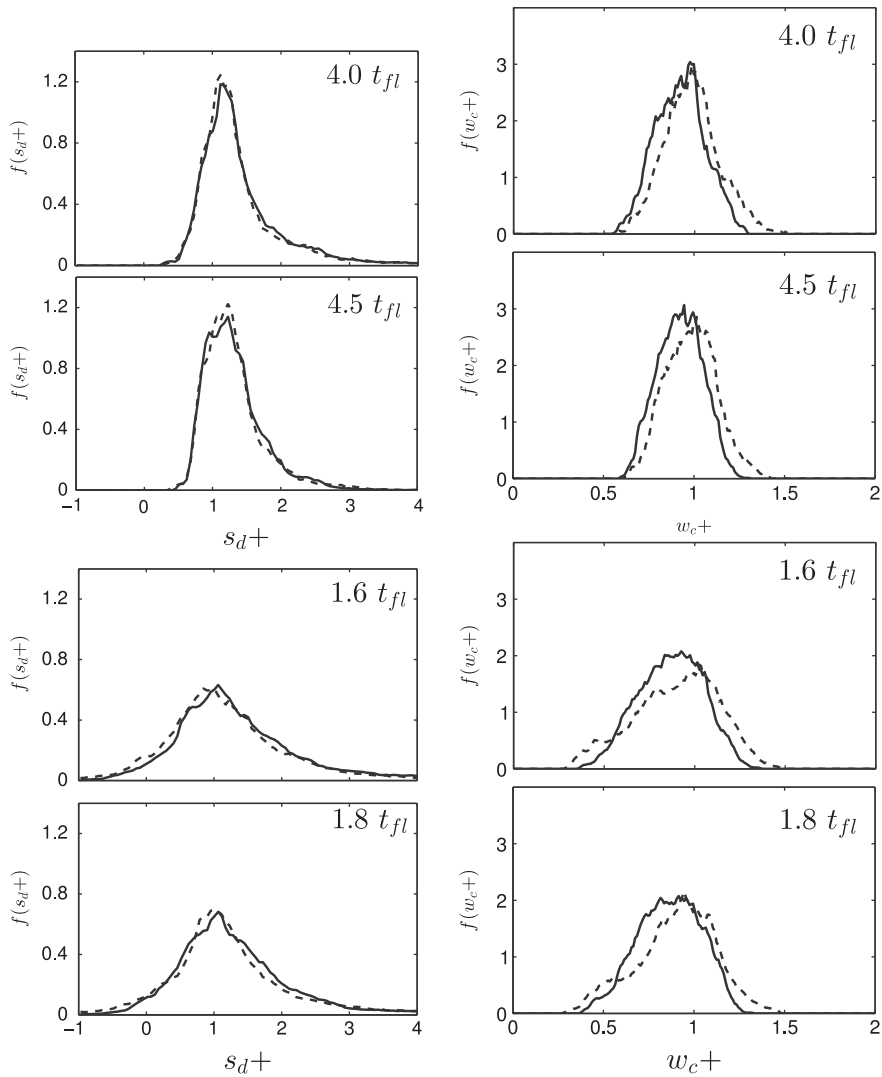


**Fig. 26.** Pdfs of $s_d^+$ and $\dot{\omega}_c^+$ for the samples collected along $c = 0.32$ iso-surface. The results are shown for two different times as noted above for case A (top row) and case B (bottom row). The solid line is for the skeletal mechanism and the dashed line is for the reduced mechanism.

both skeletal and reduced mechanism cases. The displacement speed is dictated by chemical reaction rate and the molecular diffusive fluxes as noted in Eq. (15), which are strongly coupled in premixed flames. Thus, influences of chemical kinetics, modelled using skeletal or reduced mechanism, on the propagation of the flame front, its instantaneous location and interaction with turbu-

lence are of leading order irrespective of $u_{rms}/s_l$ values. Thus, any difference one may observe in $\mathbf{x}_f$ between flames simulated using the reduced and skeletal mechanisms must originate from chemical reaction rate given by chemical kinetics and this difference is also affected by mutual interaction of turbulence and chemistry. The results in Figs. 4 and 5 show that the flame front position and, its

corrugations and contortions resulting from turbulence-flame interaction are not very different when the 5-step reduced mechanism is used instead of the skeletal mechanism. To gain a closer understanding of this behaviour, the pdfs of $s_d^+$ and $\dot{\omega}_c^+$, where $\dot{\omega}_c^+$ is the progress variable reaction rate, using the samples collected along the flame front ($c = 0.32$ iso-surface) are shown in Fig. 26. The results are shown for two different times, $t^+ \equiv t/t_{fl} = 4$ and 4.5 for case A and 1.6 and 1.8 for case B. These times, normalised by the flame time, can easily be translated in terms of initial eddy turnover time, $t_e$, since $t^+ = \hat{t}$ Da, where $\hat{t} = t/t_e$. Thus, the times shown in Fig. 26 correspond to a difference of about $0.1 t_e$. These times, sufficiently separated but close enough, are chosen carefully to avoid any bias from chemistry reduction error or insufficient turbulence–chemistry interaction. The later point is ensured by selecting $\hat{t} > 1$, which is widely accepted to be sufficient to realise a fully developed interaction between turbulence and chemistry. It is clear in Fig. 26 that the reduced chemistry represents turbulence–chemistry interaction and flame stretch effects well compared to the skeletal mechanism. It is worth to note that the values of $u_{rms}/s_l$ are of $\mathcal{O}(1)$ in case A and $\mathcal{O}(10)$ in case B. Thus, it is apparent that the 5-step reduced chemistry considered here can represent both instantaneous flame front features and flame related statistics well over a good range of turbulence level.

Despite these insights and good performances observed, one must recognise that the results reported in this study are specific to the turbulence and mixture conditions tested here. The reduced mechanism is observed to perform relatively better for the lower turbulence level considered in this study. This implies that this mechanism performs better for larger Da number flames. Its performance for the lower Da number flame, case B, is somewhat reduced and more tests with Da < 1 flames are required to make further assessment. Since the QSS assumptions hold better in the PSR limit which aided the reduced mechanism development, it is expected that there could be a regime between the PSR and flamelet combustion limits where this mechanism may have some difficulties. Thus, further DNS at higher turbulence levels is required to establish an upper limit for the applicability of this reduced mechanism. Also, additional DNS in non-premixed combustion with extinction and re-ignition, would be useful in evaluating the performance of this reduced mechanism over a broader range of conditions.

## 4. Conclusions

A direct numerical simulation was used to examine the performance of a 5-step reduced mechanism for combustion of multicomponent fuel mixtures. The DNS database includes two sets of simulations at low and high turbulence conditions, $u_{rms}/s_l \sim \mathcal{O}(1)$ and $\mathcal{O}(10)$, performed using both skeletal and reduced mechanisms developed in [36]. In this study, premixed combustion of a multicomponent fuel mixture consisting of CO, $H_2$, $H_2O$, $CH_4$ and $CO_2$ is simulated. Three dimensional homogeneous turbulence enters through one end of the computational domain and leaves from the other end after interacting with a premixed flame. The performance of the reduced mechanism is evaluated by (1) comparing cross correlations of instantaneous heat release rate and species mass fractions obtained using both the skeletal and reduced mechanisms, (2) using physical space analysis of average mass fractions and reaction rates of various species, (3) analysing flame structures in progress variable space, (4) studying scatter plots and pdfs of flame surface variables and (5) comparing normalised instantaneous displacement speed and reaction rate distributions on the flame surface.

The mean mass fractions and reaction rates of H, $O_2$, CO, $CO_2$, and $CH_4$ computed using the reduced mechanism are found to be

in agreement with those from the skeletal mechanism. A similar behaviour is observed for the correlation coefficients, see Eq. (16), for these species. The reduced mechanism slightly over-estimates the average mass fractions of $H_2O$, $H_2$, and $H_2O_2$ inside the flame brush, particularly in regions where the heat release rate peaks. The spatial cross correlation for these species is observed to be weak. This is shown to be related to the over-estimation of their reaction rates inside the flame brush. The validity of the rate-related QSS assumptions for the steady-state species in turbulent flames is also examined. It is found that the rate-related QSSA for HCO holds better for both turbulent cases than in the unstrained laminar flame. The rate-related QSS errors on the other hand, for OH, $HO_2$, O, $CH_3$ and $CH_2O$, are found not to hold as well as in the laminar case and this error peaks mainly for low $c$ values where turbulence is stronger. Despite this no direct link between the poorer spatial correlations for $H_2O$, $H_2$, and $H_2O_2$, and the increased rate-related QSS errors of the steady-state species is observed. This implies that the discrepancies in the instantaneous mass fractions of $H_2O$, $H_2$, and $H_2O_2$ are rather a manifestation of the differences in turbulence–chemistry interaction for the reduced mechanism cases resulting from turbulent diffusion and convection induced by fluctuating heat release rate.

The instantaneous contours of heat release rate are found to be very similar for the low turbulence case with high correlation coefficients. For the high turbulence case the heat release correlation is reduced and significant differences are observed in the instantaneous heat release rate contours. Nevertheless, the spatial variation of mean heat release rate and progress variable for the reduced mechanism agrees well with the skeletal mechanism results. Furthermore, the pdfs of displacement speed, curvature, tangential strain, stretch and generalized FSD are found to be nearly identical. The scatter plots of heat release rate and displacement speed against curvature and tangential strain rate are observed to be similar for the reduced and skeletal mechanism. Also, the difference in distributions of instantaneous displacement speed and heat release rate on the flame surface is observed to be small.

These results suggest that the 5-step reduced mechanism developed in [36], is a reasonable substitute for the skeletal mechanism even for the turbulent flames, at least for the conditions considered in this study. These results also suggest that the performance of the reduced mechanism is improved for the low turbulence level compared to the high turbulence level considered here. Since premixed combustion is considered for this study, direct simulations of other combustion modes such as non-premixed combustion under a wide range of flow conditions causing extinction and re-ignition events need to be performed to assess the range of applicability of this reduced mechanism. This is a subject for further study. Use of the reduced mechanism is shown to reduce the computational burdens considerably. Furthermore, the ability of the CARM [39] software to directly produce source codes for the species reaction rates makes it seamless and straightforward to include the reduced mechanism in direct numerical or large eddy simulations. Thus, a wide range of turbulence and thermo-chemical conditions can be covered for DNS of multi-component fuel combustion in archetypical configurations, which are akin to practical devices, by using the 5-step reduced mechanism.

HECToR, the UK's national high-performance computing service, which is provided by UoE HPCx Ltd at the University of Edinburgh, Cray Inc and NAG Ltd, and funded by the Office of Science and Technology through EPSRC's High End Computing Programme.

A copy of CHEMKIN compatible reaction rate subroutine from CARM for the reduced mechanism can be obtained by writing to zn209@cam.ac.uk or ZachariasMNic@gmail.com. Also available as supplementary material to this article.

## References

[1] T. Komori, N. Yamagami, H. Hara, Gas Turbine Engineering Section Power Systems Headquarters Mitsubishi Heavy Industries, Ltd. Industrial Report, <www.mhi.co.jp/power/news/Section1/pdf/2004_-nov_-04b.pdf>, Design for Blast Furnace Gas Firing Gas Turbine, 2004.
[2] Report: Hydrogen from Coal Program:Research, Development, and Demonstration Plan for the Period 2008 Through 2016, U.S. Department of Energy, 2008.
[3] Report: Wabash River Coal Gasification Re-powering Project: A DOE Assessment, U.S. Department of Energy National Energy Technology Laboratory, 2002.
[4] O. Maustard, Report: Massachusetts Institute of Technology Laboratory for Energy and the Environment, An overview of coal based integrated Gasification Combined Cycle (IGCC) Technology, 2005.
[5] U. Maas, S.B. Pope, Proc. Combust. Inst. 24 (1992) 719–729.
[6] U. Maas, S.B. Pope, Combust. Flame 88 (1992) 239–264.
[7] O. Gicquel, N. Darabiha, D. Thevenin, Proc. Combust. Inst. 28 (2000) 1901–1908.
[8] J.A. van Oijen, F.A. Lammers, L.P.H. de Goey, Combust. Sci. Technol. 127 (2001) 2124–2134.
[9] S.B. Pope, Combust. Theory Modell. 1 (1997) 41–63.
[10] B. Yang, S.B. Pope, Combust. Flame 112 (1998) 85–112.
[11] N. Peters, in: Numerical Simulation of Combustion Phenomena, Springer-Verlag, Berlin, 1985, pp. 90–109.
[12] W.P. Jones, R.P. Lindstedt, Combust. Flame 73 (1988) 222–233.
[13] T. Turanyi, A.S. Tomlin, M.J. Pilling, J. Phys. Chem. 97 (1993) 163–172.
[14] J.Y. Chen, Trans. Aeronaut. Astronaut. Soc. Repub. China 33 (2001) 59–67.
[15] J. Warnatz, U. Maas, R.W. Dibble, Combustion, third ed., Springer-Verlag, 2001. 86–88.
[16] C.J. Montgomery, C. Yang, A.R. Parkinson, J.Y. Chen, Combust. Flame 144 (2006) 37–52.
[17] C.J. Sung, C.K. Law, J.Y. Chen, Symp. Int. Combust. (1998) 295–304.
[18] A. Massias, D. Diamantis, E. Mastorakos, D. Goussis, Combust. Theory Modell. 3 (1999) 233–257.
[19] T. Lovas, D. Nilson, F. Mauss, Symp. Int. Combust. 28 (2000) 1809–1815.
[20] S. Mahalingam, J.H. Chen, L. Vervisch, Combust. Flame 102 (1995) 285–297.
[21] C.J. Montgomery, G. Kosaly, J.J. Riley, Combust. Flame 109 (1996) 113–144 (nonpremixed combustion with multistep hydrogen–oxygen kinetics).
[22] T. Echekki, J.H. Chen, Combust. Flame 106 (1996) 184–202.
[23] N. Swaminathan, S. Mahalingam, Combust. Sci. Technol. 112 (1997) 301–326.
[24] N. Swaminathan, R. Bilger, Combust. Sci. Technol. 127 (1997) 167–196.
[25] E.R. Hawkes, J.H. Chen, Combust. Flame 138 (2004) 242–258.
[26] R. Sankaran, E.R. Hawkes, J.H. Chen, T. Lu, C.K. Law, J. Phys. Conf. Ser. 46 (2006).
[27] C.S. Yoo, E.S. Richardson, R. Sankaran, J.H. Chen, Proc. Combust. Inst. 33 (2011) 1619–1627.
[28] J.H. Chen, Proc. Combust. Inst. 33 (2011) 99–123.
[29] L. Vervisch, Symp. Int. Combust. 28 (2000) 11–23.
[30] T.J. Poinsot, Symp. Int. Combust. 26 (1996) 219–232.
[31] C.K. Westbrook, Y. Mizobuchi, T.J. Poinsot, P.J. Smith, J. Warnatz, Proc. Combust. Inst. 30 (2005) 125–157.
[32] M. Baum, T.J. Poinsot, D.C. Haworth, in: Proceedings of the Summer Program, Stanford Univ. NASA-Ames, 1992.
[33] M. Baum, T.J. Poinsot, D.C. Haworth, N. Darabiha, J. Fluid Mech. 281 (1994) 1–32.
[34] N. Chakraborty, G. Hartung, M. Katraggada, C.F. Kaminski, Combust. Flame 158 (2011) 1372–1390.
[35] V. Hiremath, S.R. Lantz, H. Wang, S.B. Pope, Proc. Combust. Inst. 34 (2013) 205–215.
[36] Z.M. Nikolaou, J.Y. Chen, N. Swaminathan, Combust. Flame 160 (2013) 56–75.
[37] R.S. Cant, SENGA2 User Guide, CUED/ATHERMO/TR67, September 2012.
[38] M.D. Smooke, V. Giovangigli, in: M.D. Smooke (Ed.), Lecture Notes in Physics, vol. 384, Springer-Verlag, 1991, pp. 1–29.
[39] J.Y. Chen, Y.F. Tham, Combust. Flame 153 (2008) 634–646.
[40] Y.F. Tham, F. Bisetti, J.Y. Chen, Eng. Gas Turb. Power 130 (2008).
[41] C.A. Kennedy, M.H. Carpenter, R.M. Lewis, Appl. Numer. Math. 35 (2000) 177–219.
[42] K.W. Thompson, J. Comput. Phys. 68 (1987) 1–24.
[43] K.W. Thompson, J. Comput. Phys. 89 (1990) 439–461.
[44] J.C. Sutherland, C.A. Kennedy, J. Comput. Phys. 191 (2003) 502–524.
[45] C.S. Yoo, Y. Wang, A. Trouve, H.G. Im, Combust. Theory Model. 9 (2005) 617–646.
[46] C.S. Yoo, H.G. Im, Combust. Theory Modell. 11 (2007) 259–286.
[47] R.J. Kee, J.F. Grcar, M.D. Smooke, J.A. Miller, Tech. Rep. SAND85-8240 Sandia National Laboratories, A Fortran Program for Modelling Steady Laminar One-dimensional Premixed Flames, 1985.
[48] R.J. Kee, F.M. Rupley, J.A. Miller, Chemkin-II: A Fortran Chemical Kinetics Package for the Analysis of Gas Phase Chemical Kinetics, Sandia National Laboratories Report, SAND89-8009B, 1992.
[49] N. Peters, J. Fluid Mech. 384 (1999) 107–132.
[50] Z.M. Nikolaou, N. Swaminathan, Direct numerical simulation of multi-component fuel combustion with detailed chemistry, Combust. Flame, October 2013, submitted for publication.
[51] S.M. Candel, T. Poinsot, Combust. Sci. Technol. 70 (1990) 1–15.
[52] A.K. Das, K. Kumar, C. Sung, Combust. Flame 158 (2011) 345–353.
[53] D. Singh, N. Takayuki, T. Saad, L. Qiao, Fuel (2012) 448–456.
[54] R. Hilbert, F. Tap, H. El-Rabii, D. Thevenin, Progr. Energy Combust. Sci. 30 (2004) 61–117.